



Article

Enhanced UV-Visible Light Photocatalytic Activity by Constructing Appropriate Heterostructures between Mesopore TiO₂ Nanospheres and Sn₃O₄ Nanoparticles

Jianling Hu , Jianhai Tu, Xingyang Li, Ziya Wang, Yan Li, Quanshui Li and Fengping Wang *

Department of Physics, School of Mathematics and Physics, University of Science and Technology Beijing, Beijing 10083, China; jlhu_ustb@163.com (J.H.); jianhaituustb@163.com (J.T.); xl99936@uga.edu (X.L.); wzywolf@163.com (Z.W.); liyan000998@163.com (Y.L.); qsli@ustb.edu.cn (Q.L.)

* Correspondence: fpwang@ustb.edu.cn; Tel.: +86-10-6233-2587; Fax: +86-10-6233-2993

Received: 25 September 2017; Accepted: 13 October 2017; Published: 19 October 2017

Abstract: Novel TiO₂/Sn₃O₄ heterostructure photocatalysts were ingeniously synthesized via a scalable two-step method. The impressive photocatalytic abilities of the TiO₂/Sn₃O₄ sphere nanocomposites were validated by the degradation test of methyl orange and •OH trapping photoluminescence experiments under ultraviolet (UV) and visible light irradiation, respectively. Especially under the visible light, the TiO₂/Sn₃O₄ nanocomposites demonstrated a superb photocatalytic activity, with 81.2% of methyl orange (MO) decomposed at 30 min after irradiation, which greatly exceeded that of the P25 (13.4%), TiO₂ (0.5%) and pure Sn₃O₄ (59.1%) nanostructures. This enhanced photocatalytic performance could be attributed to the mesopore induced by the monodispersed TiO₂ cores that supply sufficient surface areas and accessibility to reactant molecules. This exquisite hetero-architecture facilitates extended UV-visible absorption and efficient photoexcited charge carrier separation.

Keywords: photocatalyst; heterostructures; TiO₂; Sn₃O₄

1. Introduction

As a stable, low-cost and environmentally benign material, nanoscaled titanium dioxide (TiO₂) with unique structural and functional properties has become a widely used semiconductor photocatalyst for various solar-driven clean energy technologies [1]. Tailoring the morphology of TiO₂ photoanode is a preferred route to achieving high performance in solar cells due to its enhanced properties, such as high surface area, faster electron transport, lower electron-hole recombination rate and good light-harvesting features [2,3]. Nevertheless, the wide optical bandgap of TiO₂, which seriously limits its light harvesting capability, leaving about 96% of the solar light energy wasted [4]. Compared with the solution of generating donor or acceptor states in the band gap by adding impurities, rationally designing and constructing the surface heterostructures would be a more efficient strategy for achieving an excellent photocatalyst [5].

Recently, Sn₃O₄, a novel non-stoichiometric oxide, has raised particular interest in the field of photocatalysis—especially in terms of its catalytic behavior under visible light irradiation—due to a suitable band-gap inside visible light (2.2–2.9 eV) and a distinct surface structure composed of both valences of tin [6,7]. Several studies have shown its great potential as an auspicious photocatalyst under visible light, both for generating hydrogen and degrading dyes [8]. However, some drawbacks have hindered its performance in practice. As a semiconductor with a relatively narrow band gap, pure Sn₃O₄ generally leads to a fast recombination of photoexcited electron-hole pairs, which ultimately decreases its degradation rate [9].

Discussing these problems together, it proposes an intriguing idea that Sn_3O_4 , as the second component, attaches to the surface of TiO_2 nanostructures, for an exquisite $\text{TiO}_2/\text{Sn}_3\text{O}_4$ heterostructure. On the one hand, a theoretical analysis indicates that the interface between TiO_2 and Sn_3O_4 is to be a perfect type-II heterojunction (both the potentials of valence band (VB) and conduction band (CB) of Sn_3O_4 are higher than that of TiO_2) [10], which is actually conducive to the separation of photoexcited electron-hole pairs. Furthermore, latest reports have exhibited the superiority of the heterogeneous composite of this kind [11,12]. On the other hand, increased photoactive facets can effectively facilitate the efficiency of photo-absorption and oxygen chemisorption, and bring about a fast rate of surface reactions [13]. Therefore, highly dispersive anatase TiO_2 mesopore nanospheres, which possess a large number of active surfaces, would likely be an amazing matrix in $\text{TiO}_2/\text{Sn}_3\text{O}_4$ nanocomposites.

The two-step self-assembly approach is a feasible strategy for the refined design of hierarchical nanostructures with complex morphologies, and has been proven to be an effective way to design multiscale nanostructures, since the morphology and composition obtained from the first step can be further tuned and adjusted by a subsequent second process. Moreover, this approach also allows the combination of multiple synthetic techniques, and the synthesis of complex nanostructures with hierarchical multiscale structures compared with the conventional one-step self-assembling method [14]. Recently, a lot of complex nanostructures with high photocatalytic performance for both visible light and ultraviolet has been acquired by the two-step synthesis method. Usually, these methods can be classified into two categories: (1) synthesis under two continuous identical methods, such as in [9,15,16]; and (2) synthesis under two different methods, such as in [17,18]. In 2015, $\text{TiO}_2/\text{Sn}_3\text{O}_4$ nanobelts [9] were successfully produced by first synthesizing the TiO_2 nanobelts, and then assembling Sn_3O_4 onto the TiO_2 nanobelts in a subsequent hydrothermal procedure; in the same year, hierarchical $\text{Sn}_3\text{O}_4/\text{N-TiO}_2$ nanotubes [17] were synthesized by first weaving N-doped TiO_2 nanotube via electro-spinning, and then modifying them with Sn_3O_4 via hydrothermal reaction. In 2017, a range of heterojunction WO_3/TiO_2 thin films were deposited via a two-step process using chemical vapor deposition (CVD) methods [15]. Generally, electro-spinning and chemical vapor deposition is associated with at least one of the following factors: expensive equipment, high voltage, hazardous by-products, or toxic chemicals, rendering the method less environmental friendly and much more complicated than the hydrothermal method or sol-gel synthesis. Hence, synthesizing complex nanostructures via a combination of sol-gel and hydrothermal methods would be a low-cost, scalable, easy to control, and eco-friendly strategy in terms of preparing high-quality, uniform, catalysts.

Herein, we developed a scalable two-step route, combining the sol-gel method and hydrothermal progress to achieve excellent visible and ultraviolet photocatalytic activity by uniformly synthesizing the Sn_3O_4 nanoparticles on the surface of TiO_2 nanospheres. As expected, an enormous enhancement of photocatalytic efficiency was achieved by the distinctive $\text{TiO}_2/\text{Sn}_3\text{O}_4$ nanocomposites.

2. Experimental Section

2.1. Chemicals

The chemicals used in this study were of analytic grade, and were used without further purification. Tetrabutyl titanate was purchased from Beijing Xingjin Chemical Factory, Beijing, China. Methyl orange (MO) was obtained from Tianjin Jinke Fine Chemical Industry Research Institute, Tianjin, China. Tin dichloride dihydrate ($\text{SnCl}_2 \cdot 2\text{H}_2\text{O}$) and trisodium citrate dihydrate ($\text{Na}_3\text{C}_6\text{H}_5\text{O}_7 \cdot 2\text{H}_2\text{O}$) were purchased from Xilong Chemical Industry Co., Ltd., Guangdong, China. Terephthalic acid was purchased from Alfa Aesar (Tianjin, China). All the other organic solvents and salts, including ethylene glycol, acetone, NaOH, were purchased from Sinopharm Chemical Reagent Beijing Co. P25 (nanoscale TiO_2 powder, surface area $50 \text{ m}^2 \cdot \text{g}^{-1}$) was purchased from Degussa AG (Hanau, Germany).

2.2. Synthesis of Samples

In this research, we propose a two-step synthesis method to obtain $\text{TiO}_2/\text{Sn}_3\text{O}_4$ nanocomposites by preparing TiO_2 core via sol-gel route first and then synthesizing Sn_3O_4 on the surface of TiO_2 . (1) Synthesis of core TiO_2 nanospheres [19]: 3.5 mL tetrabutyl titanate was dissolved in the 50 mL ethylene glycol while stirring vigorously for 10 h. Then, the mixture was immediately poured into a solution containing 170 mL acetone and 2.7 mL deionized water under constant stirring, until white precipitation appeared. The acquired precipitate was calcined in air at 500 °C for 1 h to produce the TiO_2 powders; (2) Coating TiO_2 with Sn_3O_4 : 0.2 g of the TiO_2 product described above and 5.0 mmol $\text{SnCl}_2 \cdot 2\text{H}_2\text{O}$ were mixed with 25 mL deionized water, followed by the addition of 12.5 mmol $\text{Na}_3\text{C}_6\text{H}_5\text{O}_7 \cdot 2\text{H}_2\text{O}$ and 2.5 mmol NaOH under magnetic stirring. During this process, Sn(II) ions were attached to the surface of hydroxyl-rich TiO_2 spherical colloids through inorganic grafting. The resulting precursor was then transferred to a 50 mL Teflon-lined stainless autoclave and maintained at 180 °C for 12 h. Finally, the collected powder was washed several times with deionized water and ethanol, and dried at 60 °C for 12 h.

2.3. Characterization of Samples

In order to obtain the physical and chemical properties of as-prepared samples, several characterizations were conducted. X-ray diffraction (XRD) patterns were recorded by a Rigaku D/MAX-2500 diffractometer with Cu $K\alpha$ radiation (Rigaku, Tokyo, Japan). Raman spectra were obtained using a HORIBA HR800 spectrometer with an Nd:YAG laser at a wavelength of 532 nm (Horiba Yvon, Paris, France). Scanning electron microscopy (SEM) and transmission electron microscopy (TEM) images were acquired from the ZEISS SUPRA 55 (Zeiss, Oberkochen, Germany) and JEOL JEM-2010 (JEOL, Tokyo, Japan), respectively. X-ray photoelectron spectra (XPS) were recorded on a scanning X-ray microprobe PHI Quantera II (Ulvac-PHI, Chigasaki, Japan). The nitrogen adsorption-desorption isotherm was measured at 77 K on an Autosorb-iQ2-MP analyzer (Quantachrome Instruments, Boynton Beach, FL, USA). The absorption spectra were carried out by UV-visible spectrophotometer (Lambda 950, Perkin-Elmer, Shelton, WA, USA) and the hydroxyl radicals ($\bullet\text{OH}$) trapping photoluminescence spectra were examined by a fluorescence spectrophotometer (Hitachi F-4500, Hitachi, Tokyo, Japan) using excitation a wavelength of 315 nm.

2.4. Photocatalytic Experiments

The photocatalytic activity of $\text{TiO}_2/\text{Sn}_3\text{O}_4$ nanocomposites was evaluated via methyl orange (MO) degradation rate. 80 mL aqueous suspension of MO (20 mg/L) and 80 mg of photocatalyst powder were placed in a 100 mL beaker. Prior to irradiating, the suspensions were magnetically stirred in the dark for 40 min to establish adsorption-desorption equilibrium. A 250 W mercury lamp and a 500 W Halogen lamp with a 420 nm cut-off filter were used as the UV and visible light sources, respectively. After given irradiation time intervals, aliquots of the mixed solution were collected and centrifuged to remove the catalyst particulates for analysis. Four consecutive cycles were tested. The samples were washed thoroughly with water and dried after each cycle.

Using terephthalic acid as a probe molecule, the hydroxyl radicals ($\bullet\text{OH}$) at the photo-illuminated sample/water interface were examined by a special photoluminescence (PL) technique. Terephthalic acid reacts readily with $\bullet\text{OH}$, producing 2-hydroxyterephthalic acid, a great fluorescent material with a unique photoluminescence peak at 426 nm [20], which makes it easy to detect by fluorescence spectrum (excitation wavelength: 315 nm, fluorescence peak: 426 nm). In a typical experiment, 80 mL 0.5 mM terephthalic acid and 2 mM NaOH aqueous solution were completely mixed and then transferred into a 100 mL beaker. The rest of steps are the same as for the degradation of MO.

3. Results and Discussion

Figure 1a illustrates the XRD pattern of the TiO₂/Sn₃O₄ nanocomposites. All the diffraction peaks can be indexed to the anatase TiO₂ (JCPDS 21-1272, marked with black ●) and triclinic Sn₃O₄ (JCPDS 16-0737, marked with red ☆), validating the high purity of the synthesized TiO₂/Sn₃O₄ composite phase. Compared with the single-phase TiO₂ and Sn₃O₄, all the diffraction peaks are broad and weak, which indicates that the crystallinities are slightly reduced [21]. This result may be attributed to lattice distortion induced by interfacial strain because of different lattice parameters between Sn₃O₄ and TiO₂ [22]. In addition, Raman spectroscopy results (Figure 1b) further confirm the purity of the synthesized TiO₂/Sn₃O₄ composite phase. Specifically, Raman activities of 144, 196, 396, 520 and 638 cm⁻¹ were assigned to the anatase TiO₂ [23], and the 133, 143, 170 and 238 cm⁻¹ Raman peaks could be attributed to the Sn₃O₄, in accordance with previous reports [7,24]. The textures of the as-synthesized TiO₂/Sn₃O₄, TiO₂, Sn₃O₄ and P25 were characterized by N₂ physisorption experiments. The Brunauer–Emmett–Teller (BET) surface area data of samples are provided in Table 1. The N₂ adsorption-desorption isotherm and pore-size distribution of TiO₂/Sn₃O₄ nanocomposites are shown in Figure 1c. The results display that the TiO₂/Sn₃O₄ nanocomposites possess an average pore diameter of 2.733 nm and a larger surface area of 68.1 m²/g than the as-prepared TiO₂ (0.04 m²/g), Sn₃O₄ (35.2 m²/g), and the reported TiO₂/Sn₃O₄ nanobelt heterostructure (51.5 m²/g) [9]. Such a high surface-to-volume ratio for the TiO₂/Sn₃O₄ nanocomposites might be of extreme good value in photocatalytic processes, as they would provide more active sites for the adsorption of reactant molecules, and their optical absorbance would increase at visible wavelengths [25]. Figure 1d shows the UV-visible diffusion reflectance spectra (DRS) and plots of (F(R)hv)^{1/2} versus photo energy (hv) of the TiO₂/Sn₃O₄ along with spectra of the pristine TiO₂ and Sn₃O₄ for comparison. The absorption spectra of the TiO₂/Sn₃O₄ nanocomposites exhibit the mixed absorption properties of both the components. In particular, the absorption edge for TiO₂/Sn₃O₄ nanocomposites is clearly shifted towards visible region (near 505 nm). The optical band gap determined from the plot of the Kubelka-Munk function was found to be 2.46 eV, compared to the observed values of 3.22 eV and 2.61 eV for TiO₂ and Sn₃O₄, respectively. These data reveal the Sn₃O₄/TiO₂ nanocomposites have a lower band gap than the pure Sn₃O₄ and TiO₂ nanoparticles, which is consistent with the published literature [9], and can be explained by the reduced crystallinity of both materials [1], as shown by XRD analysis.

Table 1. The specific surface area and apparent reaction rate constants (κ) of TiO₂, P25, Sn₃O₄ TiO₂/Sn₃O₄ samples.

Photocatalyst	TiO ₂	P25	Sn ₃ O ₄	TiO ₂ /Sn ₃ O ₄
	κ (min ⁻¹)	κ (min ⁻¹)	κ (min ⁻¹)	κ (min ⁻¹)
UV irradiation	0.028	0.24	0.064	0.24
Visible light	0.0010	0.0023	0.024	0.052
Surface Area (m ² ·g ⁻¹)	0.04	50	35.2	68.1

The chemical composition and valence state were characterized by X-ray photoelectron spectroscopy (XPS). The full range of XPS spectra, ranging from 0 to 1000 eV, of TiO₂/Sn₃O₄ nanocomposites are shown in Figure 2a. No impurities were observed in the spectra, which is consistent with the results of XRD and Raman. Figure 2b shows the curve fitting data of the Sn 3d core-level spectra. Moreover, the Sn 3d doublet characterized by Sn 3d_{3/2}–Sn 3d_{5/2} splitting peak can be clearly observed. The prominent peak of Sn 3d_{5/2} level is dissolved into two peaks centered at 486.77 and 486.15 eV, which can be attributed to Sn(IV) and Sn(II) configurations [26], respectively. The Sn 3d_{3/2} spectra exhibit two peaks at 495.14 and 494.51 eV, which are assigned to Sn²⁺ and Sn⁴⁺ [26]. As shown in Figure 2c, the binding energies (BE) of Ti 2p_{3/2} and Ti 2p_{1/2} are 458.5 and 464.2 eV respectively, which are ascribed to the Ti⁴⁺ oxidation states [27]. On the basis of the above discussion, it can be concluded that the TiO₂/Sn₃O₄ sample is composed of Ti(IV), Sn(II and IV), and O, which is in good agreement with the XRD and Raman results. In addition, the calculated Ti/Sn ratio is 0.20,

indicating that most of the surface of the TiO₂ nanocrystals is covered by Sn₃O₄ nanocrystals (SEM and TEM experiments further confirm this result, and will be discussed later).

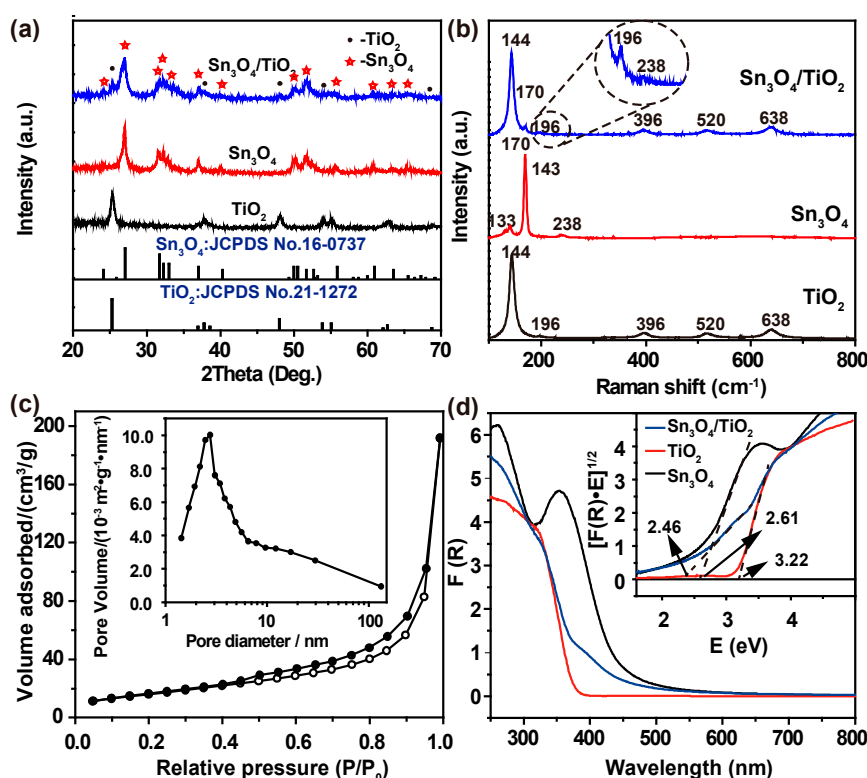


Figure 1. (a) XRD patterns, (b) Raman spectra of TiO₂, Sn₃O₄ and TiO₂/Sn₃O₄ nanocomposites, (c) N₂ adsorption-desorption isotherms of TiO₂/Sn₃O₄ nanocomposites and (d) UV-visible diffuse reflectance spectra and plots of $(F(R)hv)^{1/2}$ versus photo energy (right insert) of TiO₂, Sn₃O₄ and TiO₂/Sn₃O₄ nanocomposites.

The morphology and microstructure of the as-prepared TiO₂/Sn₃O₄ nanocomposites were carefully analyzed by microscopy. Generally, lots of interleaved Sn₃O₄ nanoplates are able to self-assemble into an ordinary flower-like nanostructure, as shown in Figure 3a. Similarly, by introducing highly monodispersed TiO₂ nanospheres of ~130 nm diameter (Figure 3b) into the growth environment, the homogeneous Sn₃O₄ nanoparticles started to grow on the surface of each individual TiO₂ core with intimate contact, thus forming an interface of two different semiconductors that would facilitate photo-excited electron transfer and photon-generated carrier separation (Figure 3c,d). Noticeably, the composites inherit a favorable dispersion in the solution, and fully contact with the absorbate, which is positive for the outstanding photocatalytic performance. However, it should be noted that the TiO₂/Sn₃O₄ nanocomposites are not completely covered by Sn₃O₄ nanocrystals. Furthermore, these advantageous heterojunctions with 10–20 nm sizes wrapping uniformly onto the surface of TiO₂ nanospheres were verified by TEM observation, as shown in Figure 1e,f. The well-resolved lattice fringes from the core and shell regions manifestly correspond to the (101) planes of anatase TiO₂ and the (210) planes of Sn₃O₄, respectively, clearly revealing the phase distribution of the TiO₂/Sn₃O₄ nanocomposites again.

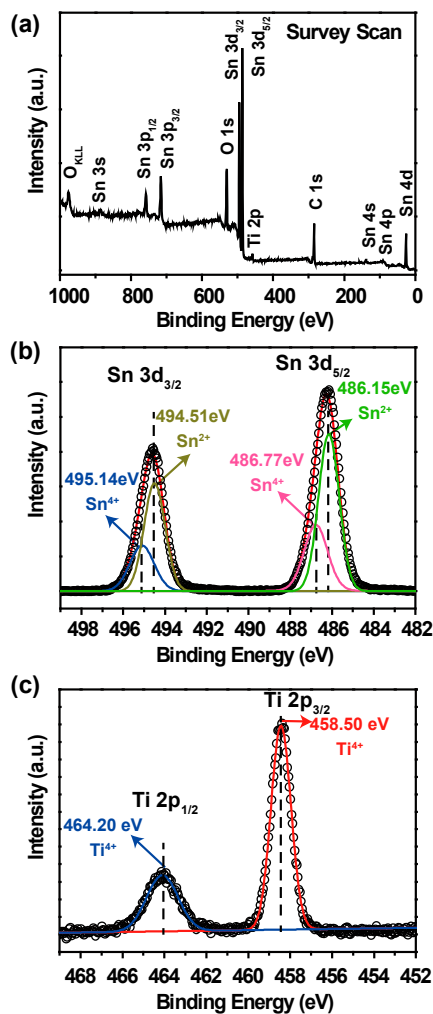


Figure 2. (a) Survey scan of XPS, (b) Sn 3d core level XPS spectra, and (c) Ti 2p core level XPS spectra of the TiO₂/Sn₃O₄ nanocomposites.

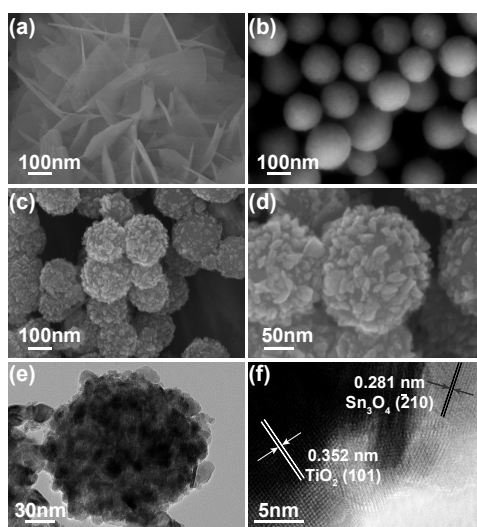


Figure 3. SEM images of the (a) Sn₃O₄, (b) TiO₂, and (c,d) TiO₂/Sn₃O₄ nanocomposites; (e) TEM and (f) HRTEM images of the TiO₂/Sn₃O₄ nanocomposites.

The photocatalytic activities of P25, TiO₂, Sn₃O₄ and TiO₂/Sn₃O₄ heterostructures were evaluated by the degradation of MO in water under UV- and visible-light irradiation (Figure 4a,b). The degradation of the MO solution under identical experimental conditions, but with no photocatalyst, is provided for comparison. The degradation efficiency of the as-synthesized TiO₂/Sn₃O₄ heterostructures was defined as C/C_0 , where C_0 is the initial concentration of MO after equilibrium adsorption, and C is the concentration during the reaction. Both blank experiment results showed that MO could not be decomposed without photocatalyst under UV- or visible-light irradiation. In contrast, the photodegradation efficiency of TiO₂/Sn₃O₄ nanocomposites was 95% within 30 min under UV-light irradiation, which is superior to the as-prepared TiO₂ nanospheres (62%) and Sn₃O₄ nanoplates (70%). Furthermore, the MO decomposition efficiency found for the TiO₂/Sn₃O₄ photocatalyst was comparable to that determined under the same experimental conditions for the reference P25 catalyst; that is, 99% after 10 min. Additionally, in the visible-light irradiation experiment (Figure 4b), the TiO₂/Sn₃O₄ nanocomposites (81%) exhibited significantly higher photocatalytic activity than P25 (9%), TiO₂ (0.4%) and Sn₃O₄ (60%) at 30 min. Finally, MO was completely degraded within 80 min. The results show that the TiO₂/Sn₃O₄ heterostructures exhibited improved photocatalytic activity.

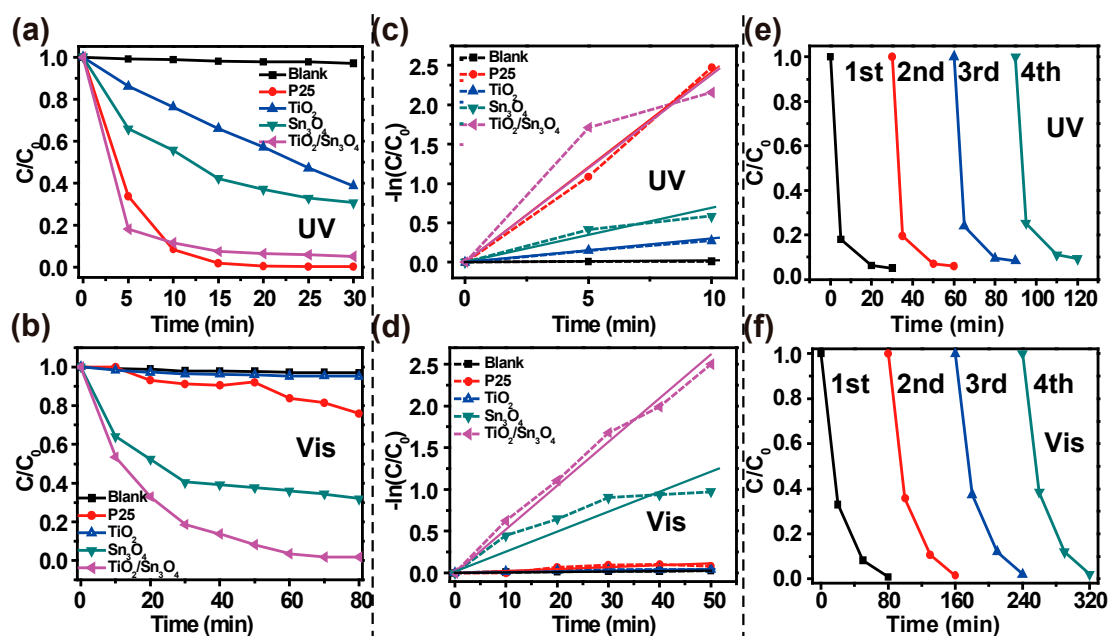


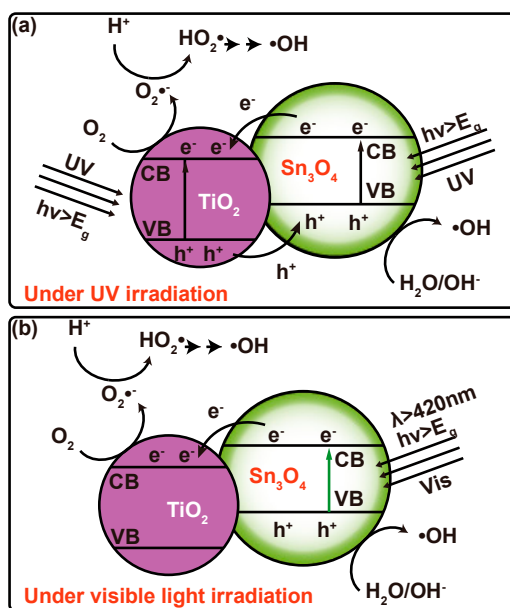
Figure 4. The photocatalytic activity (a,b), plots of $-\ln[C/C_0]$ versus irradiation time (c,d), and stability for MO photo-degradation (e,f) of TiO₂, P25, Sn₃O₄ and TiO₂/Sn₃O₄ nanocomposites under UV- and visible-light irradiation, respectively. The corresponding curves of MO without photocatalyst under UV and visible light irradiation are provided for comparison.

For a better understanding, the photocatalytic kinetics of the samples was analyzed using the Langmuir-Hinshelwood model, as shown in Figure 4c,d. All of the data follow a first-order reaction model, and the calculated apparent kinetic rate constants (κ) are summarized in Table 1. We found that, under UV irradiation, the TiO₂/Sn₃O₄ exhibited a much faster photo-decomposition activity ($\kappa = 0.24 \text{ min}^{-1}$) than the pure TiO₂ (0.028 min^{-1}) and Sn₃O₄ (0.064 min^{-1}), and was as fast as the P25 (0.24 min^{-1}). Furthermore, under visible-light irradiation, the calculated value of κ for the TiO₂/Sn₃O₄ sample ($\kappa = 0.052 \text{ min}^{-1}$) was twice as high as that for the neat Sn₃O₄ (0.024 min^{-1}), and more than a dozen times higher than that for the single TiO₂ (0.0010 min^{-1}) and the P25 ($\kappa = 0.0023 \text{ min}^{-1}$). In addition, the TiO₂/Sn₃O₄ heterostructures could be recycled and reused at least four times without significant loss of efficiency (Figure 4e,f), which demonstrates its great potential as an efficient and

stable photocatalytic material. These remarkably good performances can be attributed to the improved UV- and visible-light absorption efficiency, and the high photo-excited carrier-separation rate resulting from the novel TiO₂/Sn₃O₄ heterostructures.

Based on all of the results above, a possible mechanism for charge transfer and photocatalytic process can be proposed (Scheme 1). As illustrated in Figure 1d, the diffusion reflectance spectra (DRS) and plots of $(F(R)hv)^{1/2}$ versus photo energy (hv) indicate that the bandgap of Sn₃O₄ (2.61 eV) is smaller than that of TiO₂ (3.22 eV). Additionally, the potentials of the valence band (VB) and conduction band (CB) of Sn₃O₄ are higher than those of TiO₂, so the heterostructure of TiO₂/Sn₃O₄ belongs to typical type-II heterojunction [9]. When Sn₃O₄ contacts TiO₂ cores to form a heterojunction, the difference in chemical potential causes band bending at the interface of the junction [28], which drives photoexcited electrons to transfer from Sn₃O₄ to TiO₂, and photoexcited holes to migrate in the opposite direction, until the Fermi levels of TiO₂ and Sn₃O₄ reach equilibrium. The possible mechanisms for charge transfer and hydroxyl radical (•OH) generation under UV- and visible-light irradiation will be discussed separately. (1) Upon UV illumination, electrons in the VB could be excited to the CB of both oxides, simultaneously forming the same number of holes in the VB. This is due to the fact that the Sn₃O₄ nanoparticles were not fully coated as a shell onto the TiO₂ nanospheres (Figure 3c,d) and that the suitable bandgap of TiO₂ and Sn₃O₄ is lower than the energy of ultraviolet photons. Next, the photo-generated electrons were collected by the TiO₂ particles and the holes by the Sn₃O₄ particles; that is, electrons transferred from Sn₃O₄ to TiO₂, and holes migrated from TiO₂ to Sn₃O₄ (compare Scheme 1a with Figure 1d). The unique behavior that electrons and holes preferentially accumulate on different materials would result in a great separation of photo-generated carriers, and thus reduce the charge recombination rate, ultimately increasing carrier lifetime. As a consequence, the formation efficiency of hydroxyl radicals (•OH)—a strong oxidant for most pollutants [9,20,29]—by the reaction of holes with surface hydroxyl groups or physisorbed water molecules at the Sn₃O₄ surface and the production rates of •OH and superoxide radicals (O₂^{•−}) radicals resulting from the reactions of electrons with dissolved oxygen molecules and water molecules will be massively enhanced; this will increase the volume of oxidant inside the system. (2) Under visible-light irradiation (Scheme 1b), electrons in the VB could be exclusively excited to the CB of Sn₃O₄, with a concomitant formation of the same number of holes in the VB. Due to the type II band alignment of the as-prepared sample, the photoexcited electrons in the Sn₃O₄ CB will be easily injected into the TiO₂ CB, where the electrons could reduce surface-absorbed O₂ over TiO₂ active sites to form superoxide radicals (O₂^{•−}), and the new species can further yield •OH by reacting with water or oxidize MO. On the other hand, holes remaining in Sn₃O₄ could react with surface-absorbed H₂O to generate more •OH. Hydroxyl radicals (•OH) and superoxide radicals (O₂^{•−}) stemming from the above procedure will degrade MO into colorless chemicals, and even CO₂ and H₂O, which is similar under UV illumination. All in all, the enhanced charge separation related to the TiO₂/Sn₃O₄ heterojunction favors the interfacial charge transfer to physisorbed species, forming •OH radicals and reducing possible back reactions, and therefore accounts for the higher activity of the TiO₂/Sn₃O₄ nanocomposites.

The photocatalytic oxidation of dyes occurs through the reactive species, which came into being after the light absorption and electron-hole formation by the photocatalyst [30]. Terephthalic acid photoluminescence probing technique (TAPL) was employed to examine the generation of active •OH radicals [31]. Figure 5a,b gives the •OH-trapping photoluminescent spectra of TiO₂/Sn₃O₄ nanocomposites in TA solution with UV- and visible-light irradiation, respectively. The increased photoluminescence intensity confirms that the •OH radicals are mainly responsible for the photodegradation process, and it also verifies the photocatalytic activity of the TiO₂/Sn₃O₄ nanocomposites.



Scheme 1. Illustration of photo-induced charge transfer and separation at the interface of $\text{TiO}_2/\text{Sn}_3\text{O}_4$ hierarchical hybrid nanostructures under (a) UV- and (b) visible-light irradiation.

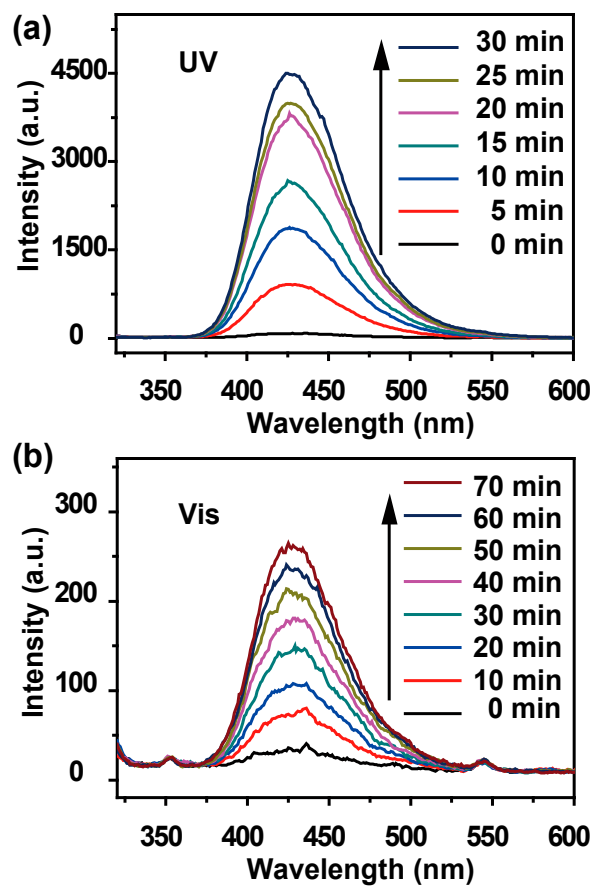


Figure 5. The $\bullet\text{OH}$ -trapping photoluminescence spectra of $\text{TiO}_2/\text{Sn}_3\text{O}_4$ nanocomposites under (a) UV- and (b) visible-light irradiation, respectively.

4. Conclusions

In summary, this study demonstrates a facile route to synthesizing TiO₂/Sn₃O₄ nanocomposites that not only display enhanced photocatalytic performance in UV irradiation, but also allow a significant level of visible light photocatalytic activity. The large surface area derived from the monodispersed mesopore TiO₂/Sn₃O₄ nanospheres and unique TiO₂/Sn₃O₄ heterojunctions are considered to be major contributions to supplying abundant active sites and separating photogenerated carriers, respectively. The strengthened photocatalytic performances will greatly promote the practical application of the TiO₂/Sn₃O₄ nanocomposites in eliminating organic pollutants from wastewater, and producing hydrogen by splitting.

Acknowledgments: We appreciate the financial support of the National Natural Science Foundation of China (Grant No. 61373072).

Author Contributions: F.W. and J.H. conceived and designed the experiments; J.H. and J.T. performed the experiments; J.H., J.T., X.L. and Z.W. analyzed the data; F.W., Q.L. and Y.L. contributed reagents/materials/analysis tools; J.H., J.T. and X.L. wrote the paper with input from all authors.

Conflicts of Interest: The authors declare no conflict of interest.

References

1. Chen, X.; Liu, L.; Peter, Y.Y.; Mao, S.S. Increasing solar absorption for photocatalysis with black hydrogenated titanium dioxide nanocrystals. *Science* **2011**, *331*, 746–750. [[CrossRef](#)] [[PubMed](#)]
2. Sun, Z.; Liao, T.; Sheng, L.; Kou, L.; Kim, J.H.; Dou, S.X. Deliberate design of TiO₂ nanostructures towards superior photovoltaic cells. *Chem.-A Eur. J.* **2016**, *22*, 11357–11364. [[CrossRef](#)] [[PubMed](#)]
3. Sun, Z.; Liao, T.; Kou, L. Strategies for designing metal oxide nanostructures. *Sci. China Mater.* **2017**, *60*, 1–24. [[CrossRef](#)]
4. Asahi, R.; Morikawa, T.; Ohwaki, T.; Aoki, K.; Taga, Y. Visible-light photocatalysis in nitrogen-doped titanium oxides. *Science* **2001**, *293*, 269–271. [[CrossRef](#)] [[PubMed](#)]
5. Zhao, Z.; Tian, J.; Sang, Y.; Cabot, A.; Liu, H. Structure, synthesis, and applications of TiO₂ nanobelts. *Adv. Mater.* **2015**, *27*, 2557–2582. [[CrossRef](#)] [[PubMed](#)]
6. Manikandan, M.; Tanabe, T.; Li, P.; Ueda, S.; Ramesh, G.V.; Kodiyath, R.; Wang, J.; Hara, T.; Dakshnamoorthy, A.; Ishihara, S. Photocatalytic water splitting under visible light by mixed-valence Sn₃O₄. *ACS Appl. Mater. Interfaces* **2014**, *6*, 3790–3793. [[CrossRef](#)] [[PubMed](#)]
7. He, Y.; Li, D.; Chen, J.; Shao, Y.; Xian, J.; Zheng, X.; Wang, P. Sn₃O₄: A novel heterovalent-tin photocatalyst with hierarchical 3D nanostructures under visible light. *RSC Adv.* **2014**, *4*, 1266–1269. [[CrossRef](#)]
8. Berengue, O.; Simon, R.; Chiquito, A.; Dalmaschio, C.; Leite, E.; Guerreiro, H.; Guimarães, F.E.G. Semiconducting Sn₃O₄ nanobelts: Growth and electronic structure. *J. Appl. Phys.* **2010**, *107*, 033717. [[CrossRef](#)]
9. Chen, G.; Ji, S.; Sang, Y.; Chang, S.; Wang, Y.; Hao, P.; Claverie, J.; Liu, H.; Yu, G. Synthesis of scaly Sn₃O₄/TiO₂ nanobelt heterostructures for enhanced UV-visible light photocatalytic activity. *Nanoscale* **2015**, *7*, 3117–3125. [[CrossRef](#)] [[PubMed](#)]
10. Wang, Y.; Wang, Q.; Zhan, X.; Wang, F.; Safdar, M.; He, J. Visible light driven type II heterostructures and their enhanced photocatalysis properties: A review. *Nanoscale* **2013**, *5*, 8326–8339. [[CrossRef](#)] [[PubMed](#)]
11. Ye, W.; Shao, Y.; Hu, X.; Liu, C.; Sun, C. Highly Enhanced Photoreductive Degradation of Polybromodiphenyl Ethers with g-C₃N₄/TiO₂ under Visible Light Irradiation. *Nanomaterials* **2017**, *7*, 76. [[CrossRef](#)] [[PubMed](#)]
12. Low, J.; Yu, J.; Jaroniec, M.; Wageh, S.; Al-Ghamdi, A.A. Heterojunction photocatalysts. *Adv. Mater.* **2017**, *43*, 5234–5244. [[CrossRef](#)] [[PubMed](#)]
13. Linsebigler, A.L.; Lu, G.; Yates, J.T., Jr. Photocatalysis on TiO₂ surfaces: Principles, mechanisms, and selected results. *Chem. Rev.* **1995**, *95*, 735–758. [[CrossRef](#)]
14. Liu, Q.; Sun, Z.; Dou, Y.; Kim, J.H.; Dou, S.X. Two-step self-assembly of hierarchically-ordered nanostructures. *J. Mater. Chem. A* **2015**, *3*, 11688–11699. [[CrossRef](#)]
15. Sotelo-Vazquez, C.; Quesada-Cabrera, R.; Ling, M.; Scanlon, D.O.; Kafizas, A.; Thakur, P.K.; Lee, T.L.; Taylor, A.; Watson, G.W.; Palgrave, R.G. Evidence and Effect of Photogenerated Charge Transfer for

- Enhanced Photocatalysis in WO₃/TiO₂ Heterojunction Films: A Computational and Experimental Study. *Adv. Funct. Mater.* **2017**, *27*. [[CrossRef](#)]
16. Nanakkal, A.; Alexander, L. Photocatalytic activity of graphene/ZnO nanocomposite fabricated by two-step electrochemical route. *J. Chem. Sci.* **2017**, *129*, 95–102. [[CrossRef](#)]
 17. Yu, X.; Wang, L.; Zhang, J.; Guo, W.; Zhao, Z.; Qin, Y.; Mou, X.; Li, A.; Liu, H. Hierarchical hybrid nanostructures of Sn₃O₄ on N doped TiO₂ nanotubes with enhanced photocatalytic performance. *J. Mater. Chem. A* **2015**, *3*, 19129–19136. [[CrossRef](#)]
 18. Nanakkal, A.; Alexander, L. Graphene/BiVO₄/TiO₂ nanocomposite: Tuning band gap energies for superior photocatalytic activity under visible light. *J. Mater. Sci.* **2017**, *52*, 7997–8006. [[CrossRef](#)]
 19. Jiang, X.; Herricks, T.; Xia, Y. Monodispersed spherical colloids of titania: Synthesis, characterization, and crystallization. *Adv. Mater.* **2003**, *15*, 1205–1209. [[CrossRef](#)]
 20. Martínez, D.S.; Martínez-De La Cruz, A.; Cuéllar, E.L. Photocatalytic properties of WO₃ nanoparticles obtained by precipitation in presence of urea as complexing agent. *Appl. Catal. A Gen.* **2011**, *398*, 179–186. [[CrossRef](#)]
 21. Cullity, B. *Elements of X-Ray Diffractions*; Addison-Wesley: Reading, MA, USA, 1978; p. 102.
 22. Sang, Y.; Yu, D.; Avdeev, M.; Qin, H.; Wang, J.; Liu, H.; Lv, Y. Yttrium aluminum garnet Nanoparticles with low antisite Defects studied with neutron and X-ray diffraction. *J. Solid State Chem.* **2012**, *192*, 366–370. [[CrossRef](#)]
 23. Khan, M.M.; Ansari, S.A.; Pradhan, D.; Ansari, M.O.; Lee, J.; Cho, M.H. Band gap engineered TiO₂ nanoparticles for visible light induced photoelectrochemical and photocatalytic studies. *J. Mater. Chem. A* **2014**, *2*, 637–644. [[CrossRef](#)]
 24. Wang, F.; Zhou, X.; Zhou, J.; Sham, T.-K.; Ding, Z. Observation of single tin dioxide nanoribbons by confocal Raman microspectroscopy. *J. Phys. Chem. C* **2007**, *111*, 18839–18843. [[CrossRef](#)]
 25. Pawar, R.; Lee, C.S. *Heterogeneous Nanocomposite-Photocatalysis for Water Purification*; William Andrew: New York, NY, USA, 2015; pp. 68–76.
 26. Wang, J.; Lu, C.; Liu, X.; Wang, Y.; Zhu, Z.; Meng, D. Synthesis of tin oxide (SnO & SnO₂) micro/nanostructures with novel distribution characteristic and superior photocatalytic performance. *Mater. Des.* **2017**, *115*, 103–111.
 27. Wagner, C.D. *Handbook of X-Ray Photoelectron Spectroscopy*; A Reference Book of Standard Data for Use in X-ray Photoelectron Spectroscopy; Physical Electronics Division, Perkin-Elmer Corporation: Eden Prairie, MN, USA, 1979; pp. 68–69.
 28. McDaniel, H.; Heil, P.E.; Tsai, C.-L.; Kim, K.; Shim, M. Integration of type II nanorod heterostructures into photovoltaics. *ACS Nano* **2011**, *5*, 7677–7683. [[CrossRef](#)] [[PubMed](#)]
 29. Dong, W.; Pan, F.; Xu, L.; Zheng, M.; Sow, C.H.; Wu, K.; Xu, G. Q.; Chen, W. Facile synthesis of CdS@TiO₂ core-shell nanorods with controllable shell thickness and enhanced photocatalytic activity under visible light irradiation. *Appl. Surf. Sci.* **2015**, *349*, 279–286. [[CrossRef](#)]
 30. Malik, V.; Pokhriyal, M.; Uma, S. Single step hydrothermal synthesis of beyerite, CaBi₂O₂(CO₃)₂ for the fabrication of UV-visible light photocatalyst BiOI/CaBi₂O₂(CO₃)₂. *RSC Adv.* **2016**, *6*, 38252–38262. [[CrossRef](#)]
 31. Cao, J.; Xu, B.; Luo, B.; Lin, H.; Chen, S. Novel BiOI/BiOBr heterojunction photocatalysts with enhanced visible light photocatalytic properties. *Catal. Commun.* **2011**, *13*, 63–68. [[CrossRef](#)]

